JOURNAL OF COMPUTATIONAL PHYSICS 49, 241–264 (1983)

Spatial Resolution Requirements for Direct Numerical Simulation of the Rayleigh–Bénard Convection

GÜNTHER GRÖTZBACH

Kernforschungszentrum Karlsruhe, Institut für Reaktorentwicklung, D-7500 Karlsruhe, Federal Republic of Germany

Received January 6, 1982; revised July 7, 1982

Three criteria are deduced for the prediction of grids, which allow for accurate direct numerical simulations of turbulent flows. These criteria are based on wavelength considerations, boundary layer thickness estimates, and on a simplified theoretical model to calculate the coefficient of a verified subgrid-scale heat flux model. The criteria have been successfully tested by comparing the results of several three-dimensional and time-dependent numerical simulations for the Rayleigh–Bénard convection of air in an infinite channel up to $Ra = 381{,}225$. Numerical results deduced from appropriate grids are in agreement with adequate experimental data. Numerical results deduced from insufficient grids show only weak deficiencies. The most sensitive data to restricted large wavelengths are the calculated Nusselt numbers and the flow regimes in the laminar-turbulent transition range; data sensitive to insufficient vertical resolution near the walls are also the Nusselt numbers; and data sensitive to insufficient horizontal resolution are the calculated Nusselt numbers and rms values of velocity and temperature fluctuations at large Rayleigh numbers. All three criteria use data specific to the type of flow only as input parameters. Therefore, these criteria may also be used for other types of flows.

1. INTRODUCTION

The investigation of Raleigh–Bénard convection between two infinite horizontal plane walls has become an important tool in studying the transition to turbulence. This is due to the simplicity of the system and due to the discrete transitions in heat transfer, which so far have not been observed in other convection systems [1]. Among the few known fully three-dimensional and time-dependent computer simulations only the work by Lipps [2] extends from the laminar to the slightly turbulent regime. The work of the author [3] extends into the fully turbulent regime.

The accuracy of these direct numerical simulations should depend only on the finite difference scheme and on the grid parameters chosen. Despite applying well known and tested schemes and grids which should be appropriate for the transition range, Lipps states a strong influence of the chosen periodicity lengths or wavelengths on the calculated frequencies and heat transfer. The problem associated with high Rayleigh number simulations conducted by the author is the large number of

0021-9991/83/020241-24$03.00/0

calculations needed to show the adequacy of the small scale resolution capabilities of the grids used.

In this paper spatial resolution requirements for the selection of appropriate grids will be deduced from physical arguments. For accurate simulation, the length scales observed in turbulent convection require very large numbers of mesh cells, which are mostly beyond the capabilities of present computer systems. For efficient numerical simulation one is interested in finding grids recording only the most important scales but, nevertheless, producing accurate results. The criteria formulated will be applied to the numerical results of the author referred to above. New results from additional simulations with the TURBIT-3 computer code [4] will also be given. These show the method is well behaved even for grids not exactly meeting all criteria. A theoretical way of testing grids in advance of application is also shown. Thus, for further simulations there is nearly no need for any check of the adequacy of the resolution capabilities of the grids used.

2. The Method of Direct Numerical Simulation

The basic equations are the conservation equations for mass, momentum, and heat. For the sake of simplicity, the validity of the Boussinesq approximation is assumed. Cartesian coordinates are used with x_1 and x_2 horizontal and x_3 directed upwards. For normalization we use the plate spacing D, the wall temperature differential ΔT_w, the velocity $u_0 = \sqrt{g\beta\,\Delta T_w D}$, the time scale $t_0 = D/u_0$, and the pressure scale $p_0 = \rho u_0^2$, where g = gravity, β = volume expansion coefficient, ρ = density. The resulting dimensionless numbers are the Reynolds number, $\mathrm{Re}_0 = u_0 D/\nu$, the Prandtl number, $\mathrm{Pr} = \nu/a$, and the Rayleigh number, $\mathrm{Ra} = g\beta\,\Delta T_w D^3/(\nu a)$, where ν = kinematic viscosity and a = temperature conductivity.

There are several ways to formally deduce a finite difference scheme for the basic equations. For a review of the methods which have become important for direct numerical simulation it is referred to the papers by Love [5] and Schumann *et al.* [6]. In the TURBIT-3 code, the box filtering method is applied in the special variant of Schumann [7]. Following the recent results by Antonopoulos-Domis [8], this method seems to have major advantages over the methods using nonlinear filters.

The procedure starts with a formal integration of the basic equations over grid volumes $v = \Delta x_1\,\Delta x_2\,\Delta x_3$. Application of the volume-averaging operator to partial derivatives of any quantity y directly produces a finite difference operator for surface averaged values, averaged over one surface ${}^iF = v/\Delta x_i$ of a mesh cell

$$\frac{1}{v}\int_v \frac{\partial y}{\partial x_i}\,dv = \frac{1}{\Delta x_1\,\Delta x_2\,\Delta x_3}\int_{\Delta x_1}\int_{\Delta x_2}\int_{\Delta x_3}\frac{\partial y}{\partial x_i}\,dx_3\,dx_2\,dx_1$$

$$= \frac{\overline{{}^v\partial y}}{\partial x_i} = \frac{1}{\Delta x_i}\left({}^i\bar{y}\left(x_i + \frac{\Delta x_i}{2}\right) - {}^i\bar{y}\left(x_i - \frac{\Delta x_i}{2}\right)\right) = \delta_i\,{}^i\bar{y}. \qquad (1)$$

The operator splits the velocity and temperature fields into spatial averages, ${}^{j}\bar{u}_j$, ${}^{v}\bar{T}$, with typical wavelengths larger than Δx_i, which are directly resolved by the grid, and into "subgrid scale" parts, $u_j' = u_j - {}^{j}\bar{u}_j$, $T' = T - {}^{v}\bar{T}$, with wavelengths smaller than Δx_i, which are not spatially resolved by the grid. Application of this operator to the basic conservation equations provides the following finite difference formulae:

$$\delta_i \, {}^{i}\bar{u}_i = 0, \qquad i = 1, 2, 3, \tag{2a}$$

$$\frac{\partial \, {}^{v}\bar{u}_i}{\partial t} + \delta_j \, {}^{j}\bar{u}_i \, {}^{j}\bar{u}_j + \delta_j \, \overline{{}^{j}u_i' u_j'} = \delta_j \left(\frac{1}{\mathrm{Re}_0} \overline{\frac{{}^{j}\partial u_i}{\partial x_j}} \right) - \delta_i \, {}^{i}\bar{p} - \frac{\mathrm{Ra}}{\mathrm{Re}_0^2 \, \mathrm{Pr}} \Delta \, {}^{v}\bar{T} \, \delta_{i3}, \tag{2b}$$

$$\frac{\partial \, {}^{v}\bar{T}}{\partial t} + \delta_j \, {}^{j}\bar{u}_j \, {}^{j}\bar{T} + \delta_j \, \overline{{}^{j}u_j' T'} = \delta_j \left(\frac{1}{\mathrm{Re}_0 \, \mathrm{Pr}} \overline{\frac{{}^{j}\partial T}{\partial x_j}} \right). \tag{2c}$$

These averaged equations are the exact results of formal volume averaging. The continuity equation is even numerically exact if a staggered grid is used. This requires a few additional linear average $\bar{y}^j$ in the convective terms in order to approximate variables between two nodes. Second-order approximations are introduced for the remaining derivatives. This holds true also for the explicit finite difference scheme, written here without space averaging bars where the superscript n refers to the time step, $t^n = n \, \Delta t$:

$$(\tilde{u}_i^{n+1} - u_i^{n-1})/(2\Delta t) = -\delta_j (\bar{u}_j^i \bar{u}_i^j)^n + \delta_j \left(\frac{1}{\mathrm{Re}_0} \delta_j u_i - \overline{{}^{j}u_i' u_j'} \right)^{n-1}$$

$$- \frac{\mathrm{Ra}}{\mathrm{Pr} \, \mathrm{Re}_0^2} ({}^{v}\bar{T}_{\mathrm{ref}} - {}^{v}\bar{T})^n \, \delta_{i3}, \tag{3a}$$

$$(T^{n+1} - T^{n-1})/(2\Delta t) = -\delta_j (u_j \bar{T}^j)^n + \delta_j \left(\frac{1}{\mathrm{Pr} \, \mathrm{Re}_0} \delta_j T - \overline{{}^{j}u_j' T'} \right)^{n-1}, \tag{3b}$$

$$\delta_i \delta_i p^n = \delta_i \tilde{u}_i^{n+1}/(2\Delta t), \tag{3c}$$

$$u_i^{n+1} = \tilde{u}_i^{n+1} - (2\Delta t) \, \delta_i p^n. \tag{3d}$$

The pressure p^n is determined from Poisson equation (3c) so that the new time level velocities u_i^{n+1} satisfy continuity equation (2a). Equation (3c) is solved by a fast Fourier transform. Equations (3a) and (3b) correspond to a leapfrog scheme starting with an Eulerian step and interrupted by an averaging step after every n_L time steps (typically, $n_L = 40$). For details of the complete scheme see, e.g., [3, 4].

Equations (2a) to (2c) look like the Reynolds equations deduced by time averaging. In the Reynolds equations, models must be introduced for the unknown shear stresses which contain the total information on turbulence. The Daly model [9] is such a statistical model. It applies seven additional transport equations for the unknown turbulence quantities.

Equations (2a)–(2c) are not averaged over time, but only over the mesh cell volumes. Therefore, the unknown terms $\overline{{}^{j}u_i' u_j'}$ and $\overline{{}^{j}u_j' T'}$ contain only the small-scale

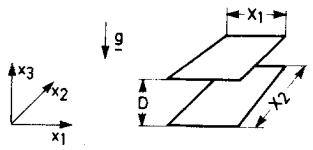

FIG. 1. Channel geometry and coordinate system.

information on turbulence, which cannot be spatially resolved by the grid used. Larger turbulence elements are resolved by the grid and will be described by the numerical scheme. Here, we neglect the subgrid-scale terms

$$^{j}\overline{u_i' u_j'} = {}^{j}\overline{u_j' T'} = 0. \tag{4}$$

However, this requires grids resolving even the smallest influential scales of the flow. Further simplifications of Eqs. (1)–(4), which would contradict the three-dimensional and time-dependent nature of turbulence, are not allowed as they would force the model to produce results of purely mathematical interest [10]. All models using a scheme for the complete basic equations and neglecting the subgrid-scale terms are called "direct numerical simulation models". The Lipps model [2] and the TURBIT-3 version used here belong to this class of models.

The boundary conditions are chosen to record the classical Rayleigh–Bénard problem in an infinite horizontal channel. Due to limited computer capabilities, we only handle a small control volume, $V = X_1 X_2 D$, for which we use periodicity boundary conditions in both horizontal directions with periodicity lengths X_1 and X_2 (Fig. 1). At both walls we assume no slip and apply linear finite difference approximations to the diffusive terms to calculate the wall shear stresses τ_{wi} and the wall heat fluxes, q_{wi}. The wall conditions for the lower wall are, e.g.,

$$\tau_{w1} = -\frac{1}{\mathrm{Re}_0} \frac{^{3}\overline{\partial u_1}}{\partial x_3} \approx \frac{-2}{\mathrm{Re}_0 \Delta x_3} {}^{1}\bar{u}_1|_1 \tag{5}$$

$$q_{w1} = -\frac{1}{\mathrm{Re}_0 \mathrm{Pr}} \frac{^{3}\overline{\partial T}}{\partial x_3} \approx \frac{-2}{\mathrm{Re}_0 \mathrm{Pr} \Delta x_3} ({}^{v}\bar{T}|_1 - T_{w1}), \tag{6}$$

where ${}^{1}\bar{u}_1|_1$ and ${}^{v}\bar{T}|_1$ are the local and time-dependent values for the grid cells adjacent to the wall. The wall temperatures T_{wi} are prescribed to be constant in time and space.

3. Spatial Resolution Requirements

Up to this point, not a single adjustable parameter appeared in the model. However, we made some important approximations of limited validity: the assumption of horizontal periodicity, the linear wall approximations in Eqs. (5) and

(6), and neglecting the subgrid-scale terms in Eqs. (2)–(6). Therefore, the next step must be the selection of grids, which are in accordance with the requirements arising from these approximations:

(i) The periodicity lengths X_i must be chosen large enough to record all relevant large-scale vortices.

(ii) The vertical grid width distribution must be able to resolve the steep gradients in the velocity and temperature fields near the walls.

(iii) The mean grid widths must be smaller than the smallest relevant turbulence elements.

Quantifying these qualitative criteria can be a serious problem. Values of X_i can be chosen on the basis of some experimental information on the wavelength λ, but no experience is available in direct simulation which would actually allow the selection of a special value. The values of Δx_3 could be chosen in the light of experience with statistical turbulence models. But due to local fluctuations of all quantities around their mean values, direct simulation can furnish much higher instantaneous values of gradients close to the wall. Values of the mean grid width could be chosen on the basis of the Kolmogorov length scale η, but grids determined in this way would involve enormous computing efforts and would not account for the very low significance of the subgrid-scale terms near the limit to total resolution. Coarser grids would only minimally detract from the accuracy of the results, but would considerably reduce the computing effort. In this section, quantitative requirements will be formulated for the criteria given above and will be applied to the grids used with TURBIT-3 for simulation of the Bénard convection. In Section 4, we will investigate these requirements on the basis of several results of these numerical simulations.

3.1. *Case Specifications*

Several simulations with different grids and different Rayleigh numbers have been performed for a Prandtl number of $\mathrm{Pr} = 0.71$ (Table I). One set of simulations, Cases 2–14, have been taken from [3]. For the two laminar cases with $\mathrm{Ra} = 4000$ and 7000, grids have been used with $N1 = N2 = 16$ nodes in both horizontal directions and $N3 = 8$ nodes in the vertical direction. The same grid has also been used for a turbulent flow with $\mathrm{Ra} = 87{,}300$, i.e., Case 4. For the other cases, including the highest Rayleigh number of 381,225, nonequidistant vertical grid width distributions are used and the node number is increased by a factor of two in each case up to $64 \times 32 \times 32$ nodes. In the second set with the new simulations, Cases 15–18, grids have been used which record twice the (periodicity) lenghts of the former simulations in each horizontal direction. For this purpose the horizontal node numbers $N1$ and $N2$ of Cases 15–18 are twice those of Cases 2, 3, 6, and 12, leaving the other grid data unchanged.

The number of time steps Nt necessary for the random initial data to reach fully developed flow is between one and five thousand. The Nt needed for Cases 13 and 14

TABLE I

Case Specifications, Grid Parameters, and Simulation Times

Case	Ra	$N1$	$N2$	$N3$	t_{max}	Nt	CPU time min	CPU time IBM
2	4000	16	16	8	71.5	1060	16	168
3	7000	16	16	8	84.9	1060	16	168
4	87,300	16	16	8	85.4	1060	16	168
5	87,300	16	16	8	84.1	1200	17	168
6	87,300	16	16	16	33.5	1880	55	168
7	381,225	16	16	16	41.0	1320	39	168
9	381,225	32	16	16	26.9	920	58	168
12	381,225	32	32	16	100.7	3680	254	3033
13	381,225	32	32	32	42.7	5040	706	3033
14	381,225	64	32	32	32.7	3880	1087	3033
15	381,225	64	64	16	66.8	2640	696	3033
16	87,300	32	32	16	73.5	4160	268	3033
17	7000	32	32	8	262.1	3960	128	3033
18	4000	32	32	8	161.4	2600	84	3033

Note. Cases 2–14 use periodicity lengths $X_1 = X_2 = 2.8$, Cases 15–18 use $X_1 = X_2 = 5.6$.

has been reduced considerably by increasing the channel mean turbulence energy in both first restart files after two hours of computing time [11]. All simulation times, in addition to the startup time, include a certain time interval in which the flow statistically is a steady-state flow. This is necessary to analyze time averages from the time-dependent results. The computation times needed for these simulations extend between 16 min on the IBM 168 and 18 h on the IBM 3033 (the latter machine being about twice as fast).

3.2. *Selection of Periodicity Lengths*

The largest scales to be recorded by the control volume V may be measured by the wavelength λ observed in turbulent convection experiments. The experimental results of Willis *et al.* [12] in the stability map by Clever and Busse [13] in Fig. 2 show decreasing wave numbers k or increasing wavelengths λ for increasing Rayleigh numbers. Thus, V should grow with λ, and so should the computing effort. For the simulations at hand this effort was restricted by assuming that it should be sufficient to have only one wavelength within the control volume, i.e., $X_1 = N1\,\Delta x_1 = X_2 = N2\,\Delta x_2 = \lambda$. Two values have been selected. For the former set of simulations the smallest appropriate value was chosen, which is $X_{1,2} = 2.8$ for the smallest Rayleigh number Ra = 4000, and was kept constant for Cases 2–14. For the new set of simulations the largest appropriate value was chosen which belongs to the largest Rayleigh number Ra = 381,225. Following the extrapolation curve for the wavelength by Daly [9], it was indicated to use $X_{1,2} = 5.6$ for Cases 15–18.

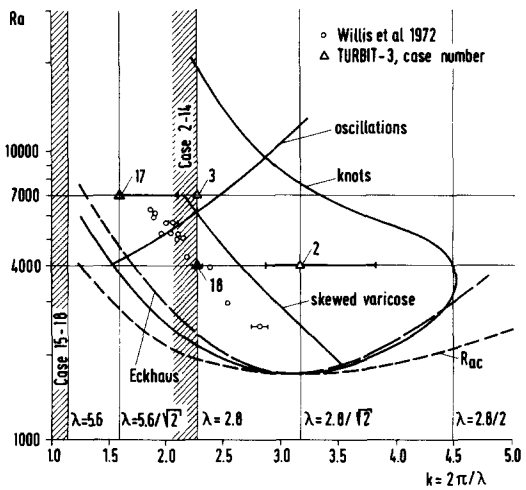

FIG. 2. Stability map for convection in air [13]. The shaded region with $\lambda > 2.8$ cannot be recorded by the grids chosen for Cases 2–14, and the region with $\lambda > 5.6$ cannot be recorded by the grids of Cases 15–18.

One consequence of applying such small periodicity lengths is that no flow regime can be calculated with $\lambda > X_i$ or $k < 2\pi/X_i$. Thus, the numerical results for cases with $\mathrm{Ra} > 4000$ and $X_i = 2.8$ may be influenced by wavelengths which are too small. Another consequence is the restriction that in case of regular flow patterns only special wavelengths, such as $\lambda = X_1$, can be calculated for λ around X_i if the axes of the vortex system run parallel to the X_2 axis, or $\lambda = X_1/\sqrt{2}$ if the vortex axes run diagonal through the grid, or $\lambda = X_1/2$ if there are two vortex pairs, etc.

3.3. *Selection of Vertical Grid Width Distributions*

Criterion (ii) requires an adequate vertical grid width distribution near the walls to justify the linear wall approximations for the diffusive terms in Eqs. (5) and (6). As is known from experiments, e.g., [14], the temperature gradients near the walls are very steep. This requires a very fine vertical resolution near the wall. Farther away from the wall, a sharp transition to the isothermal core is found in the mean temperature profile, and between both critical regions, many statistical turbulence data have sharp peaks. If it is the purpose of a simulation to study such data, very fine vertical resolution should also be used in these regions.

Statistical methods usually use at least two or three nodes within the conductive sublayer $\delta = 1/(2\,\mathrm{Nu})$, where Nu = Nusselt number, to calculate the wall fluxes. Two nodes are selected for laminar flow and three nodes for turbulent flow conditions to account for the greater local variations in the temperature field near the wall in turbulent flows. No additional requirements follow from the formulation of the wall shear stresses in Eq. (5) as we study the convection with a Prandtl number near unity.

TABLE II

The Vertical Grid Widths Δx_{3w} near the Wall Required ($\Delta x_{3w\max}$) and Actually Used (Δx_{3w}).

Case	Ra	Nu	$\Delta x_{3w\max}$	Δx_{3w}
2, 18	4000	1.97	0.1269	0.125
3, 17	7000	2.31	0.1082	0.125
4	87,300	4.70	0.0355	0.125
5	87,300	4.70	0.0355	0.0625
6, 16	87,300	4.70	0.0355	0.02
7–12, 15	381,225	7.12	0.0234	0.02
13, 14	381,225	7.12	0.0234	0.01

Note. Nu was calculated by the correlation given in [15].

To predict the maximum allowable grid widths $\Delta x_{3w\max.}$, for the cases specified in Table I, the Nusselt number is calculated by the correlation given in [15] in accordance with the calculated Nusselt numbers discussed in Section 4. The results are shown in Table II together with the Δx_{3w} values actually used. The values used are below those required for all cases except for Cases 4 and 5. Full information on the nonequidistant vertical grid width distribution is given in [3] for Cases 5–12 and in [11] for Cases 13 and 14.

3.4. *Selection of Mean Grid Widths*

Criterion (iii) in general requires a mean grid width capable of resolving the smallest scales of turbulence to justify neglecting the subgrid-scale terms (Eq. (4)). It is known for any type of turbulent flow that the smallest turbulence elements observable decrease in size with increasing turbulence level (see, e.g., [16]). For Bénard convection conditions, this has also been found in [14]. In addition, Krishnamurti [17], e.g., determined decreasing periods of oscillation for increasing Rayleigh numbers, and Fitzjarrald [18] found an increasing importance of higher frequencies in the turbulent heat flux. This has also been predicted by the optimum theory [19]. Thus, we must use decreasing mean grid widths for increasing Rayleigh numbers. This means that predictions are required for the grid widths necessary for efficient and accurate direct numerical simulation of turbulent convection.

In many publications, e.g., in the recent one by Chapman [20], the Kolmogorov length, $\eta = (\nu^3/\varepsilon)^{1/4}$, where ε is the dissipation of kinetic turbulence energy, has been used as a measure for the smallest relevant scales to estimate the magnitude of the node numbers necessary for turbulent shear flow simulation. The basis of this approach is the experience that the maximum in the dissipation spectrum $\varepsilon(k) = 2\nu k^2 E(k)$, where $E(k)$ is the spectrum of the kinetic energy $E = \langle u_i'^2 \rangle/2$, for several types of flows is at a wave number of about $k \approx 0.1/\eta$ and that the energy and dissipation spectra sharply decrease in the wave number range $0.1/\eta < k \leqslant 1/\eta$ [16]. This has also been found in Bénard convection experiments [14]. The spectra of shear stresses $E_{ij}(k)$, with $i \neq j$, are only associated with wave numbers $k \ll 1/\eta$,

because these spectra decrease much more steeply than the energy spectra with $i=j$ [21]. Thus, neglecting the subgrid-scale terms in Eq. (4) requires grids which account for a maximum wave number of about $1/\eta$.

Following Lilly [22], the maximum wave number to be recorded by the grid is $k_{max}=\pi/h$, where $h=(\Delta x_1\,\Delta x_2\,\Delta x_3)^{1/3}$ is the mean grid width. This wave number must be greater than $1/\eta$ and greater than $1/\eta_T$, where $\eta_T=(a^3/\varepsilon)^{1/4}$, which is due to the temperature field. This results in the following restrictions on mean grid widths:

$$h \leqslant \pi\eta = \pi(\nu^3/\varepsilon)^{1/4} \qquad \text{for} \quad \mathrm{Pr} \leqslant 1, \tag{7}$$

$$h \leqslant \pi\eta_T = \pi(a^3/\varepsilon)^{1/4} \qquad \text{for} \quad \mathrm{Pr} \geqslant 1. \tag{8}$$

The vertical dissipation profile is known from experiments [14] to be very flat with the exception of the regions near the walls. Therefore, here is the dissipation assumed to be constant and approximated by equalizing it to the production term due to buoyancy forces in the kinetic energy equation. With the normalization used here, Eqs. (7) and (8) are replaced by these requirements:

$$h \leqslant \pi \left(\frac{\mathrm{Pr}^2}{\mathrm{Ra\,Nu}}\right)^{1/4} \approx 4.758\,\mathrm{Pr}^{1/2}\,\mathrm{Ra}^{-0.3205}, \tag{9}$$

$$h \leqslant \pi \left(\frac{1}{\mathrm{Ra\,Pr\,Nu}}\right)^{1/4} \approx 4.758\,\mathrm{Pr}^{-1/4}\,\mathrm{Ra}^{-0.3205}. \tag{10}$$

In both equations, the Nusselt number correlation given in [15] is used, which is valid for high Prandtl numbers. For $\mathrm{Pr} \lesssim 1$, more appropriate correlations should be used. The required mean grid widths predicted are listed in Table III. The corresponding node numbers are calculated for prescribed periodicity lengths $X_1=X_2=2.8$, and for the $N3$ values given in Table I. Comparison of the two tables leads to the conclusion that the grids used for Cases 2, 3, 13, 14, and 16–18 have sufficient spatial resolution.

TABLE III

Required Mean Grid Widths and Horizontal Node Numbers Calculated from Eqs. (9) and (16)

		Eq. (9)		Eq. (16)	
Ra	$N3$	h	$N1=N2$	h	$N1=N2$
4000	8	0.2809	7	0.3992	4
7000	8	0.2348	9	0.3337	6
87,300	8	0.1046	29	0.1486	18
87,300	16	0.1046	21	0.1486	13
381,225	16	0.0652	43	0.0927	25
381,225	32	0.0652	30	0.0927	18

Note. $N1$ and $N2$ are related to h and $N3$ by $N1=N2=\sqrt{X_1X_2D/(h^3N3)}$.

Another approach to determine more efficient mean grid widths has been developed in [21]. It has been used successfully for direct and large eddy simulations (which means simulations including subgrid scale models) of temperature fluctuations in liquid metal flows [23] and for determining the mean grid widths necessary for direct numerical simulation of convection layers heated internally [24]. This approach is based on the subgrid-scale models available in the TURBIT-3 code (see, e.g., [4, 23]) and on a theoretical method of calculating the coefficient C_2 of the model for the subgrid scale momentum fluxes [7], and C_{T2} for the subgrid-scale heat fluxes [21]. The equations of definition are deduced for these proportional factors from the conservation equations for subgrid-scale kinetic energy ${}^{v}\overline{E'}$, and temperature variances, $E_T = \langle {}^{v}\overline{T'^2} \rangle$,

$$C_2 = \frac{\langle {}^{v}\bar{\varepsilon} \rangle - \nu \langle \bar{D}^2 \rangle}{\langle \overline{{}^{ij}C({}^{j}F^{j}\overline{E'})^{1/2}{}^{j}} \bar{D}^2 \rangle}, \tag{11}$$

$$C_{T2} = \frac{\langle {}^{v}\bar{\varepsilon}_T \rangle - a \langle \bar{D}_T^2 \rangle}{\langle {}^{j}C_T({}^{j}F^{j}\overline{E'})^{1/2}{}^{j}\bar{D}_T^2 \rangle}. \tag{12}$$

By $-j$ we denote linear averaging over two neighbouring values in the j direction, $\langle\ \rangle$ indicates time averages, $\bar{D}^2 = \overline{(\delta_j {}^{i}\bar{u}_i + \delta_i {}^{j}\bar{u}_j)^{j}}\, \delta_j {}^{j}\bar{u}_i$, ${}^{j}\overline{E'}$ is the subgrid-scale kinetic energy within the mesh cell surface ${}^{j}F$, ε_T is the dissipation of temperature variances, and $\bar{D}_T{}^2 = \overline{\delta_j {}^{j}\bar{T}^{j}}\, \delta_j {}^{j}\bar{T}$. The coefficients ${}^{ij}C$ and ${}^{j}C_T$ correct for geometrical anisotropies of the grid. They depend on grid parameters only and are of the order of one. In both equations, the denominator is proportional to the subgrid-scale production, the production due to subgrid-scale buoyancy forces being neglected in Eq. (11), and the numerator contains the subgrid-scale dissipation written as the difference between total dissipation and dissipation resolved directly. So, we look for the mean grid width which reduces the numerators of both equations to zero.

To determine this value we assume the subgrid-scale turbulence, which is only associated with high wave numbers, to be independent of boundary conditions, thus allowing it to be regarded as locally isotropic. Consequently, all two-point correlations of velocities, $\overline{{}^{j}u_i\, {}^{1}u_k}(\underline{\Delta x})$, and of temperatures, $\overline{{}^{i}\bar{T}^{j}\bar{T}}(\underline{\Delta x})$, which appear in Eqs. (11) and (12) by multiplying the finite difference formulas, can be calculated by the theory of isotropic turbulence on the basis of Kolmogorov's and Batchelor's energy spectra [16]. After lengthy analysis one obtains

$$C_2 \approx \frac{1 - \nu a \Gamma(1/3)(18/55)\, h^{-4/3} \langle \varepsilon \rangle^{-1/3}\, D12(\underline{\Delta x})}{(a\Gamma(1/3))^{3/2}(18/55)(9/20)^{1/2} f_1(\underline{\Delta x})}, \tag{13}$$

$$C_{T2} \approx \frac{1/2 - a\beta\Gamma(1/3)(9/20)\, h^{-4/3} \langle \varepsilon \rangle^{-1/3}\, DT2(\underline{\Delta x})}{\beta a^{1/2}((9/20)\, \Gamma(1/3))^{3/2} f_2(\underline{\Delta x})}. \tag{14}$$

The new quantities are the Kolmogorov constant $\alpha = 1.5$ and the Batchelor constant $\beta = 1.3$; the four additional functions depending on the grid width $\underline{\Delta x}$ contain a larger number of double and triple integrals, some of which can only be

evaluated numerically. For an isotropic grid, e.g., we have $D12 = 6.73$ and $DT2 = 1.66$. Thus, we can determine the mean grid width for an isotropic grid by setting the numerators of Eqs. (13) and (14) equal to zero. With the normalization used here, and with the constant dissipation approximation given above, this yields

$$h \leqslant 5.13 \left(\frac{\nu^3}{\varepsilon}\right)^{1/4} = 5.13 \left(\frac{\mathrm{Pr}^2}{\mathrm{Ra\,Nu}}\right)^{1/4} \approx 7.77 \mathrm{Pr}^{1/2} \mathrm{Ra}^{-0.3205}, \tag{15}$$

$$h \leqslant 3.45 \left(\frac{a^3}{\varepsilon}\right)^{1/4} = 3.45 \left(\frac{1}{\mathrm{Ra\,Pr\,Nu}}\right)^{1/4} \approx 5.23 \mathrm{Pr}^{-1/4} \mathrm{Ra}^{-0.3205}. \tag{16}$$

As a result of different coefficients, the left side of Eq. (15) is valid for $\mathrm{Pr} \leqslant 0.59$; that of Eq. (16) for $\mathrm{Pr} > 0.59$. Because of this very difference in the coefficients, this approach seems to be more appropriate than the criteria given in Eqs. (7) and (8), because many published large eddy simulations with this molecular Prandtl number had to use a turbulent Prandtl number for the subgrid-scale fluxes, $\mathrm{Pr}_{t\mathrm{SGS}} \approx C_2/C_{T2}$, of about 0.4 to get satisfactory results (an overview is given in [21]). We predict for coarse grids and an infinite Rayleigh number $\mathrm{Pr}_{t\mathrm{SGS}} = 0.43$ [6]. These values indicate that more stringent requirements should exist as a consequence of neglecting the subgrid-scale heat fluxes than due to the momentum fluxes.

The functional dependence of the criteria given in Eqs. (15) and (16) is the same as that of the "Kolmogorov criteria" in Eqs. (7)–(10). The coefficients are slightly larger, therefore allowing for coarser grids (Table III). The difference between both criteria seems to be small, but due to the N^4 dependence, the computing time necessary is considerably reduced by a factor of 4.2 for $\mathrm{Pr} = 0.71$. Both criteria prescribe sufficiently small mean grid widths, because the calculated values are considerably lower than the shortest wavelengths of 0.2 observed by Deardorff and Willis [14] for an even higher Rayleigh number of $\mathrm{Ra} = 6.3 \times 10^5$. Comparing Table I and the results of the criteria in Eq. (16) in Table III shows a highly insufficient spatial resolution to be predicted only for Cases 7 and 9, a moderately insufficient resolution for Cases 4 and 5. The other cases use grids, which are fine enough.

With increasing anisotropy of the grids, the values of $D12$ and $DT2$ decrease. The lowest values calculated for the grids used here are those for the mesh cells adjacent to the walls in Case 13, where $D12 = 5.0$ and $DT2 = 1.33$. This would decrease by 22% the mean grid width predicted in Eq. (15) and by 15% that predicted in Eq. (16). Thus, in case of highly anisotropic grids, it would be worthwhile to use the full theory to calculate $D12$ and $DT2$ for every type of mesh cell.

As examples of such tests of grids, the calculated coefficients C_{T2} for Cases 7–14 are given in Fig. 3 together with the terms of the kinetic energy equation calculated from Case 14. The dissipation profile increases steeply near the wall; it is constant and approximately comparable to the production term over about 60–70% of the inner part of the channel. There we find sufficient agreement with the renormalized data from [14], which apply to different Rayleigh and Nusselt numbers. The diffusion term is not very accurate in the inner part of the channel; the time interval considered

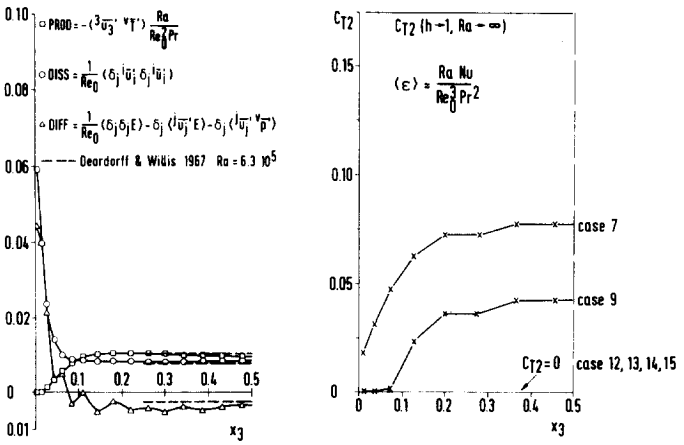

FIG. 3. Calculated terms of the turbulence energy equation for Case 14 and calculated subgrid-scale coefficient; Ra = 381,225.

is too short for accurate time averaged values to be obtained for the convective fluxes containing the energy and, especially, the pressure fluctuations, which predominantly contain low-wave number fluctuations [11]. Here we approximate the dissipation profile by a constant value, as discussed above. The resultant coefficient, C_{T2} is about 0.18 in case of very rough grids and infinite Rayleigh number. For Case 7, C_{T2} has reduced to less than 50% of this value in the center of the channel, where the grid is coarser than in the outer part, where C_{T2} decreases. For Case 9, C_{T2} has reduced to 25%, and for Cases 12–15, the result calculated is zero. These exact results are seen to agree with the isotropic-grid estimates in Eq. (16) as shown in Table III. This also holds for the cases with Ra = 87,300, where zero values of C_{T2} have been calculated only for the entire channel in Cases 6 and 16.

4. Discussion on the Basis of Numerical Results

4.1. *Influence of Periodicity Lengths*

In Section 3.2, we discussed that the shorter periodicity lengths chosen for the simulations may be appropriate only for the case with Ra = 4000, the larger one may be appropriate up to the highest Rayleigh number under consideration. The wavelengths actually calculated with both types of grids are shown in Fig. 2. For Ra = 4000, Case 2, we do not find the expected value, but a wavelength corresponding to a diagonal arrangement of a vortex pair in the grid. The flow regime should be the skewed varicose. The expected wavelength is found, however, for the large periodicity-length case, Case 18, and the same Rayleigh number. The wavelength corresponds to a system of two vortex rolls with the axis parallel to one

of the horizontal coordinates. For Ra = 7000, Case 3, the maximum recordable wavelength is found in the flow regime of oscillations.

The wavelength found for the large periodicity-length case with the same Rayleigh number, Case 17, scatters around the experimental data and the theoretical value for a diagonal arrangement of a vortex pair in the grid.

The flow regime really calculated for Ra = 4000, Case 2, as identified by contour line plots of the velocity fields indeed is the skewed varicose [3]. This regime was predicted to exist also for this Prandtl number [13]. Usually, the skewed varicose is an instability which, in experiments without controlled initial conditions, causes a new vortex system with greater wavelengths [1]. So far, the numerical result agrees with the predictions, but within the last half of the problem time, the velocity fields calculated show only minor changes and no transition to another regime. The reason for this steady-state nature of the skewed varicose may perhaps be found in the restrictions to discrete values for λ and to special spatial directions for the vortex axes. Both restrictions may prevent the instability from growing. This argument could also explain the multiplicity of stable states observed in low aspect ratio experiments within the Rayleigh number of time-independent convection [25].

A confirmation for these arguments can be given by the results of the large periodicity-length case with the same Rayleigh number, Case 18. As for all cases quasi-random initial conditions are used, both flows have to start with short wavelengths with $\lambda \gtrsim 2\Delta x$ and have to develop flow regimes with larger wavelengths.

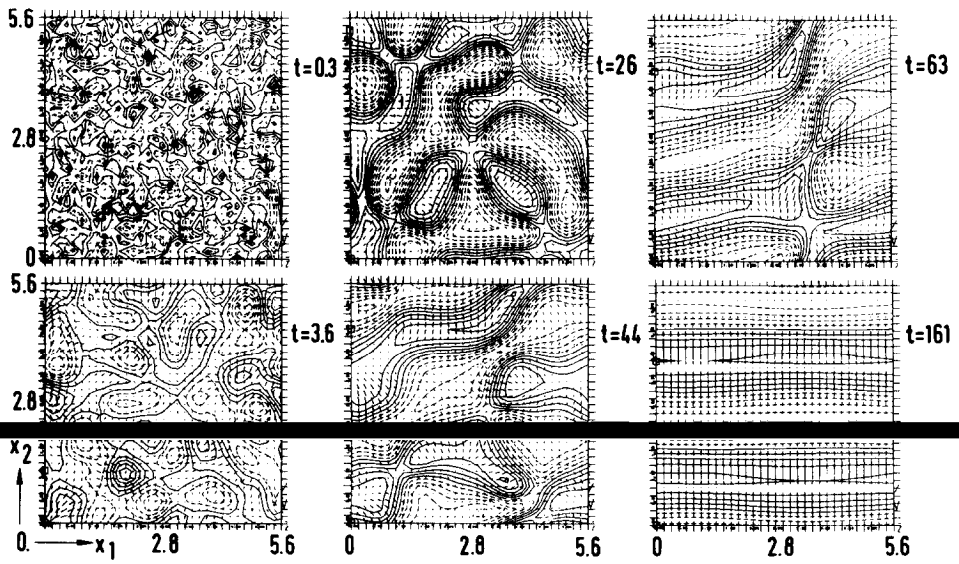

FIG. 4. The velocity field for Ra = 4000, Case 18, at $x_3 = 0.438$ showing the formation of a regular vortex roll structure. The maximum velocity vector length VVM is (in chronological order) 0.0029, 0.0022, 0.18, 0.19, 0.16, and 0.097. The contour line increment Δ is 0.0025 for $t < 3.7$, and 0.05 for $t > 3.7$.

Whereas the flow formation in Case 2 stops with stationary and regular skewed varicose like rolls, the flow formation in Case 17 passes this instability at time $t \approx 44$. Afterwards, two pairs of regular, two-dimensional, and stationary rolls are formed showing the expected wavelength $\lambda = 2.8$. This flow development can be identified by the contour line plots of the velocity fields for different time steps in Fig. 4. These are instantaneous horizontal sections through the velocity field near the midplane of the channel. We indicate equal negative vertical velocities (···) and nonnegative vertical velocities (—). The short single lines represent velocity vectors within the plane of plotting.

The flow regime calculated for Ra = 7000, Case 3, can be identified by the velocity fields given in Fig. 5. The periodic arrangement of positive and negative vertical velocities shows that one pair of rolls has developed in the control volume. Its axis of rotation is arranged parallel to the x_1 axis and is deflected in the x_2 direction. The place of maximum deflection, which is marked by circles on any contour line, travels in the negative x_1 direction through the channel causing an oscillation, as was to be expected from the stability map. Superimposed to this travelling wave with the period τ_{trans} we find an oscillation in the amplitude of deflection with a smaller period τ_{ampl}, and an oscillation in the propagation velocity of the wave with the same period τ_{ampl}.

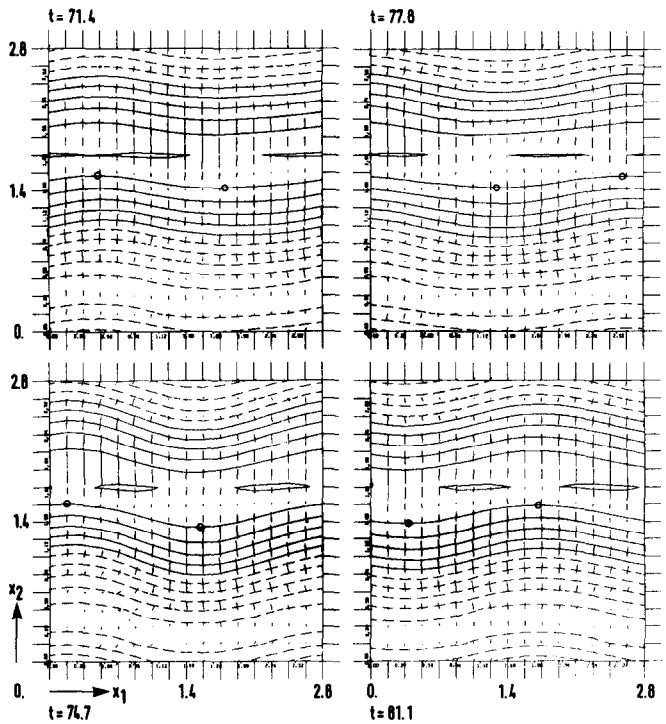

FIG. 5. Velocity field for Ra = 7000, Case 3, at $x_3 = 0.438$ showing the bimodal travelling oscillations. VVM ≈ 0.15, $\Delta = 0.05$.

Obviously, an energy exchange exists between the transport velocity of the wave and its amplitude of deflection: The amplitude of deflection is large in time intervals with low transport velocity and vice versa. The amplitude oscillates between $0.12 \times D$ and $0.24 \times D$. Thus we find a bimodal convection with accelerating and decelerating travelling waves and changing curvatures. This is precisely the flow regime observed by Krishnamurti [17] at moderate Prandtl numbers; following her data and flow regime map, this bimodal periodic convection could indeed exist for air at this Rayleigh number.

The calculated flow development for the large periodicity-length case with $\mathrm{Ra} = 7000$, Case 17, is shown in Fig. 6. For times below $t \approx 50$ the flow regimes are dominated by short wavelengths and look similar to those for Case 18. The dominant wavelengths increase with time up to $t \approx 180$ showing a cross-roll like structure at $t \approx 75$ and a diagonal roll structure for $t > 110$. Later on local discharges of hot or cold fluid from the walls cause structures with smaller scales without altering

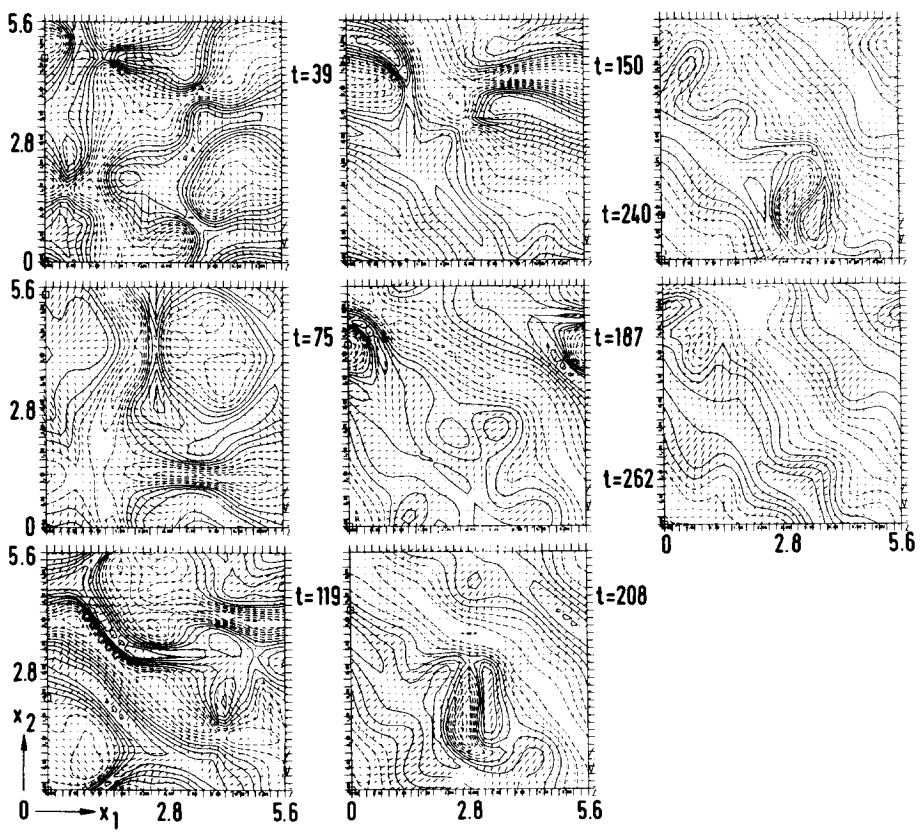

FIG. 6. Velocity field for $\mathrm{Ra} = 7000$, Case 17, at $x_3 = 0.438$ showing the formation of turbulent convection with irregular vortex roll structures; VVM is about 0.23 and $\Delta = 0.0625$.

considerably the diagonal arrangement of the large scale vortex rolls. The flow is irregular, three dimensional, and aperiodic in time; therefore it can be regarded as a turbulent flow. This flow, and the bimodal oscillatory flow found for Case 3 are really "time-dependent and three dimensional" as they should be found following the flow regime map of Krishnamurti [17]. The sensitivity of the flow regimes against periodicity lengths found here is in accordance with the large uncertainties in the flow regime bounds and in the knowledge about their dependence on aspect ratio, initial conditions, and sidewalls as discussed in [1]. The numerical results indicate the periodicity length or aspect ratio to be a dominant parameter.

One calculated instantaneous velocity field for Ra = 381,225 and for the finest grid (Case 14) is shown in Fig. 7. This horizontal section represents a highly irregular flow field; and as the flow is also aperiodic in time, one may assume that, in accordance with the flow regime map of Krishnamurti [17], really turbulent convection is simulated. The areas with positive vertical velocities form islands completely surrounded by areas with negative vertical velocities. This means that irregular cells are formed with upward flows within the cells and downward flows on their surfaces. Therefore, this may be called cellular turbulent convection. On the other hand, there are very narrow areas with negative vertical velocity, but with nearly no horizontal velocity, which may be an indication of a convection like a spoke pattern. The results found for the corresponding large periodicity-length case, Case 15, are very similar to those in Fig. 7 except that the scales have been enlarged by the ratio of the periodicity lengths used. Thus, a final conclusion on the real name for the flow regime can neither be reached for the numerical results, nor is there any unique statement on flow regimes observed experimentally for these parameters [10, 18].

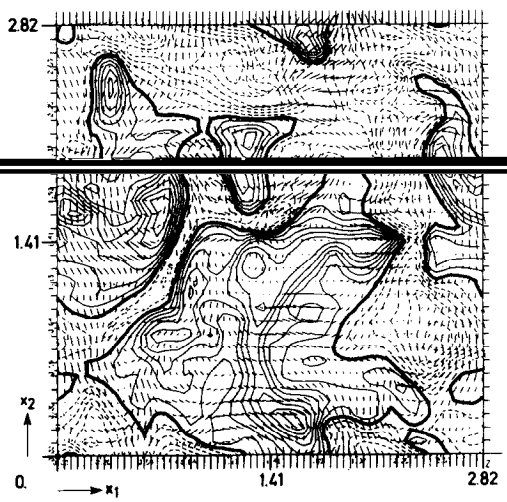

FIG. 7. Velocity field for Ra = 381,225, Case 14, at $x_3 = 0.48$ and $t = 32.8$, showing the cellular turbulent convection. VVM = 0.348 and $\Delta = 0.0625$.

For the travelling waves at Ra = 7000, some additional data can be analysed from Fig. 5 and from some more plots of this type for other times. The period τ_{ampl} of the oscillating amplitude of deflection is about 0.1 ± 0.03 in terms of the viscous diffusion time D^2/ν. It agrees quite well with one of the interpolation curves by Krishnamurti [26]. The period τ_{trans} of the travelling waves is 0.17 ± 0.03. This value is somewhat below the second curve by Krishnamurti and also slightly lower than the value $\tau = 0.19$ observed by Lipps [2]. Since he stated a strong influence of the prescribed initial wavelengths or the periodicity lengths, and here shorter periodicity lengths are used, the slightly short periods observed may be attributed to the periodicity lengths used being too short.

The calculated Nusselt numbers are compared with empirical correlations in Fig. 8. All numerical results from cases with sufficiently small grid widths and short periodicity lengths, Cases 2–14, follow the interpolation curve by Busse and Whitehead [15] quite well. However, this curve holds for Prandtl numbers above twenty. The other curves for the Prandtl number of air result in lower Nusselt numbers. It has been discussed in [2, 3] that more appropriate results could be obtained by applying greater periodicity lengths, because it is known from experiments, e.g., [18, 27], and from the overview in [28] that the Nusselt number increases with decreasing aspect ratio. Indeed, this dependence can be shown with the numerical results of the large periodicity-lengths cases, Cases 15–18. The Nusselt numbers calculated from these simulations are smaller than those of the other cases. The difference between the results from both types of grids decreases with increasing Rayleigh number because the macroscopic length scale λ also increases whereas a fixed value for the periodicity lengths has been used in the simulations. Thus, it is consistent that the experimental results by Threlfall [27] come closest to the

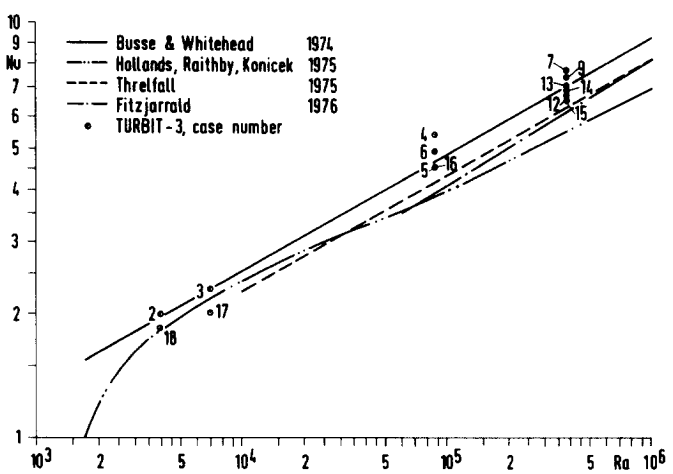

FIG. 8. Comparison between calculated Nusselt numbers and empirical correlations for air. The curve by Busse and Whitehead is for Pr = 20 to 200.

numerical results, because these experiments were performed in a cylindrical vessel with a comparable aspect ratio. The small deviations remaining may be explained by the periodicity lengths being still too small for both large Rayleigh numbers, by the shear stresses at the vertical walls missing in the calculations, and by statistical errors.

4.2. *Influence of Vertical Grid Width Distribution*

The Nusselt number is the quantity, which should react most sensitively to insufficient resolution by the vertical grid widths, as it is directly calculated from the temperature profile close to the wall. From Fig. 8, it becomes obvious that, in accordance with Table II, the result of the roughest grid for Ra = 87,300 (Case 4) is insufficient due to the vertical grid width near the wall being too large. The result for the next finer grid (Case 5) is below that for the finest grid (Cases 6 and 16), despite a vertical resolution also insufficient. The reason for this scattering is the short time interval used for time averaging of these results obtained at low Rayleigh numbers [3]. The decrease of the Nusselt number from Case 7–12 for the highest Rayleigh number cannot be caused by the vertical grid widths, as these cases use identical vertical grid with distributions. A systematic change from Case 12–14 cannot be observed. Thus, all grids used for the highest Rayleigh number seem to have a sufficient resolution near the wall. This confirms the predictions in Table II.

Another sensitive quantity is the temperature profile. The vertical profile given in Fig. 9 has been calculated from the time-dependent three-dimensional temperature field by averaging over horizontal planes and over finite time intervals; such averages

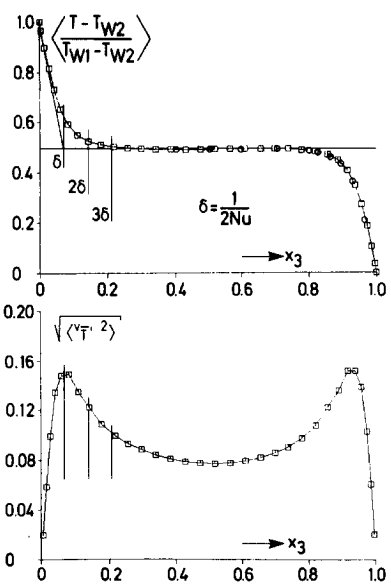

FIG. 9. Vertical time mean temperature and temperature rms-value profiles for Ra = 381,225, Case 14. (○), Deardorff and Willis, 1967, Ra = 6.3×10^5; (□), TURBIT-3, Case 14, Ra = 3.8×10^5.

are denoted by $\langle T \rangle$. The symbols on the calculated vertical mean temperature profile indicate the centers of the nodes used for Case 14. Comparison with the experimental data by Deardorff and Willis [14] for a slightly higher Rayleigh number makes it evident that enough nodes have been used in the conductive sublayer δ and in the following two or three thermal boundary layer thicknesses to resolve adequately the steep temperature gradient near the wall and its sharp transition to the isothermal core. The slight gradient reversal calculated in the inner half of the channel has also been verified, like the time mean temperature profile calculated with the coarser grid of Case 9 [3].

The vertical grid width distribution of the coarse grid of Case 9 and also that used for $\mathrm{Ra} = 87{,}300$ have been found to be of moderate accuracy for determining the position of the maximum of statistical turbulence data like the rms value of temperature fluctuations $T' = T - \langle T \rangle$ [3]. Figure 9 indicates that this problem can be removed, if necessary, by using the finer vertical resolution of grid 14. Enough nodes are used here within the first two thermal boundary layer thicknesses to adequately describe the physical profile by the volume averaged variables, and also profiles of other statistical turbulence data, such as terms of the kinetic energy equation in Fig. 3 or pressure terms [11, Appendix].

4.3. *Influence of the Mean Grid Width*

The mean grid width necessary for direct simulation of turbulent convection will be investigated by numerical results for the highest Rayleigh number because, for these cases, the strongest influence of the neglected subgrid-scale terms can be expected.

A qualitative test of the mean grid widths used can be performed by comparing, e.g., calculated instantaneous isotherm fields. Vertical sections through the temperature fields for Cases 7, 9, and 14 are contained in Fig. 10 for arbitrary times and locations. Hot thermals can be observed to rise from the lower heated wall, cold ones to fall from the upper cooled wall. The field for the roughest grid (Case 7) looks

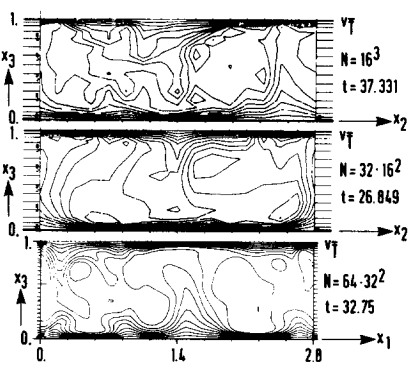

FIG. 10. Vertical sections through instantaneous isotherm fields for Case 7 at $x_1 = 0.525$, for Case 9 at $x_1 = 0.2904$, and for Case 14 at $x_2 = 0.2904$; $\mathrm{Ra} = 381{,}225$, $\Delta = 0.0625$. The short lines at the boundaries denote the sizes of mesh cells.

angular and not very reasonable. The field for Case 9 uses the same discretization in the plane of plotting as that for case 7; nevertheless, the scales and typical forms of the structures in this field seem to be more comparable to those with the finest discretization. However, when comparing the smallest horizontal scales observed at the finest grid to the horizontal grid width of the coarser grids, one must conclude that the grid of Case 9 is below or around the limit of total resolution of all small scales. The additional comparison of the horizontal grid widths used in Case 9 with the scale of the narrow structures in the horizontal section through the velocity field calculated on the finest grid in Fig. 7 clearly shows that the horizontal resolution of Case 9 is insufficient. This figure also indicates sufficient resolution by the finest grid.

The calculated Nusselt numbers have been discussed in Sections 4.1 and 4.2 (Fig. 8). For an unchanged vertical grid width, a decrease was found in the Nusselt number from Cases 7–12 which is only accompanied by a decrease of the mean grid width. In Fig. 11, the calculated Nusselt numbers and the maximum rms values of the vertical velocity and temperature fluctuation profiles are given as a function of the vertically averaged mean grid width $\bar{h} = \sqrt[3]{\Delta x_1 \Delta x_2 D/N3}$. The error bars indicated are due to time averaging over short time intervals [3]. This figure indeed illustrates that the grids of Cases 7 and 9 use too large $\bar{h}$-values, as was predicted by the "anisotropic-grid criterion" of Eq. (14) or by the "isotropic-grid criterion" of Eq. (16). The "Kolmogorov criterion" of Eq. (9) requires too little grid width, because Cases 12–14 show no systematic decrease of the Nusselt number with decreasing mean grid width. The decrease of the Nusselt number from Case 9 to the others is about 7% and in the temperature rms value about 4%. The very weak influence of the mean grid width on the rms values and the moderate one on the

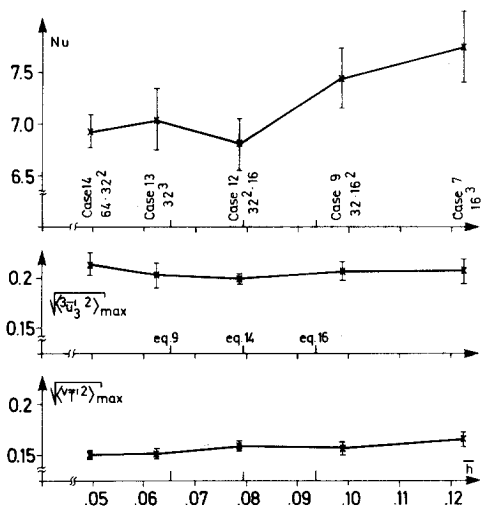

Nusselt number are the strongest influences to be detected from all calculated statistical data.

Energy spectra calculated from the spatial distribution of temperature fluctuations for Cases 9 and 14 are compared in Fig. 12. The energy of temperature variances $E_{TT} = \langle T'^2 \rangle$ is spread over 2.6 orders of magnitude on the grid of Case 9 and over 5.4 orders of magnitude on the grid of Case 14. The energy associated with the highest recordable wave number of Case 9 agrees quite well with the corresponding value of Case 14. The energy contribution above this limiting value is much less than 1%. This small value, which is not recorded by Case 9, nevertheless is of great importance. It causes inequality between turbulence production, which is totally resolved because it is mainly at low wave numbers, and turbulence dissipation, which is only partly resolved by the grid because it is at high wave numbers. As a result, the model predicts larger turbulence quantities, including turbulent heat fluxes, in case of insufficient spatial resolution (Fig. 11).

There is some discussion in the literature on the question whether the spectra for turbulent convection are continuous or whether there exist discrete peaks at discrete wave numbers [14, 19]. Both types of spectra have been observed in experiments. Here we calculate for all turbulent flows spectra decreasing continuously without any discrete peaks (Fig. 12). The same type of spectra have also been predicted for a similar problem of turbulent convection in a horizontal fluid layer with internal heat sources [24]. The type of spectra determined will strongly depend on the evaluation procedure applied. In experiments, measurements are often performed with moving probes along horizontal lines, or even measurements at single points. One-dimensional energy spectra deduced from such data must record very long time intervals to be accurate, because the time scales are very large and there are gross scale structures more or less fixed spatially, especially in experiments with low aspect ratios. When evaluating simulation results one can avoid this problem by calculating spectra from all data within a plane parallel to the walls, e.g., the data along the $N2$

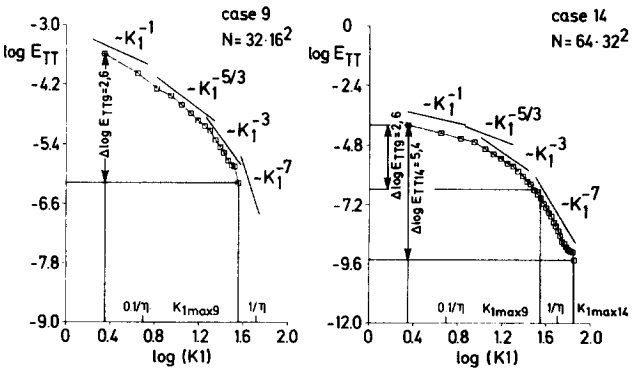

FIG. 12. Energy spectra of temperature fluctuations for Cases 9 and 14 calculated at $x_3 \approx 0.04$. Here η is determined from the local value of the dissipation profile given in Fig. 3. The maximum recordable wave number is $K_{1\,\max} = \pi/\Delta x_1$.

lines in the x_1 direction. These results in addition are averaged over time by evaluating the simulation results at eight Eulerian time steps for Cases 9 and 31 for Case 14. Thus, due to the ergodic theorem, it may be expected that continuous spectra should also be obtained by long-time averaging of experimental data.

Some evidence of the reliability of the calculated continuous spectra may be found by investigating the slopes in these spectra. The slopes and transition points observable in both spectra agree roughly (Fig. 12). There is an indication of a -1 slope corresponding to the von Karman spectrum for the low-wave number range near the walls where the production predominates (for available theories and data on spectra, see, e.g., [16]). In accordance with the results in [14] an inertial subrange with $-5/3$ slope cannot be observed; obviously, the Rayleigh number is too low to separate the dissipation range considerably from the production range. The maximum in the dissipation spectrum for temperature variances $\varepsilon_T(k) = 2ak^2E_{TT}(k)$ corresponds to a -2 slope in the E_{TT} spectrum. This slope is passed in the range of wave numbers of $0.1/\eta < K_1 \lesssim 0.2/\eta$. A result not really expected is the existence of a -3 slope; usually this is found in the inertial diffuse subrange for fluids with low Prandtl numbers. At high wave numbers around $1/\eta$ we find a slope steeper than or equal to -7, as was to be expected. This is analogous to the Heisenberg spectrum for the kinetic energy. Further spectra for the variables u_i, p, T, E calculated for Case 14 at this position and others in the channel are shown and discussed in [11].

Detailed results for the Rayleigh number $\mathrm{Ra} = 87{,}300$ are described in [3]. No systematic influence of the mean grid width has been found in any of the calculated data. Thus, the main result of this paragraph is that the anisotropic-grid criterion of Eq. (14) and also the isotropic-grid criterion in Eq. (16) together with the $DT2$ value for the nonuniform mesh really predict efficient and sufficient mean grid widths.

5. Conclusions

Three criteria have been formulated and tested, which allow for the selection of grids adequate for direct numerical simulation:

Criterion (i) requires great periodicity lengths in the horizontal directions to record the longest wavelengths observed. The grids with short periodicity lengths exactly meet this criterion at the lowest Rayleigh number. Nevertheless, the skewed varicose instability found by starting from random initial conditions cannot develop the expected wavelength because of the wavelength restrictions by the grid. The periods of the bimodal travelling waves observed at the next higher Rayleigh number are also slightly too short. The simulations with large periodicity lengths show none of these deficiencies. Thus, for simulation in the transition range, one should use periodicity lengths about two times the expected values. For turbulent flows, the insufficiently large periodicity lengths used cause the Nusselt number to be 3–5% above experimental values. This tendency is shown to be due to the analogous influence of the aspect ratio observed in experiments. For more accurate results, one should use greater periodicity lengths with about two times the expected wavelength. For the

highest Rayleigh number considered here $X_i \approx \lambda$ is used. In order to decrease the 3–5% deviation we should have used node numbers and CPU times a factor of 4 higher.

Criterion (ii) requires a fine resolution of the region near the wall due to the linear wall approximations introduced. The grids applied to simulations of turbulent convection use between 1 and 5 nodes within the thermal boundary layer thickness δ. It must be concluded from the numerical results that the calculated Nusselt number reacts sensitively to increasing the node number from 1 to 3 within δ. Further increases have no significant influence on the accuracy of the numerical results. Thus, for $Pr \gtrsim 1$, it is sufficient to use about three nodes in the vertical direction within the thermal boundary layer thickness. If it is the purpose of a simulation to investigate statistical data of turbulence, about the same number of nodes should also be used within each of the next two thermal boundary layer thicknesses to record adequately the sharp peaks or transitions in many statistical data of turbulence in this range. For Prandtl numbers considerably below unity, one must consider the viscous sublayer thickness instead of the thermal boundary layer thickness.

Criterion (iii) in general requires very fine grids to resolve the smallest scales of turbulence, because the subgrid-scale terms have been neglected. The numerical simulations performed at the highest Rayleigh number show only small deficiencies in case of grids which are too coarse. For these coarse grids, the Nusselt number and the rms values of velocity and temperature fluctuations, which have been found to be the most sensitive results, both increase only slightly with decreasing node number. The three finest grids sufficiently resolve the smallest scales of turbulence. The "Kolmogorov criteria" of Eqs. (7) and (8) prescribe very low values for the required mean grid widths. The "isotropic-grid criteria" of Eqs. (15) and (16) predict larger required grid widths, which allows for more efficient simulation of comparable accuracy than the "Kolmogorov criteria." The advantage of this method is that it may also be applied in its complete form of Eqs. (13) and (14) to test highly anisotropic grids in advance of numerical simulations.

The three criteria tested here with Bénard convection may also be applied to other types of flows, because information specific to the type of flow is only used as empirical or estimated input data. The criteria have also been verified against the simulations of internally heated convection layers [24]. A linear dissipation profile was formulated for the prediction of the mean grid width distribution. The validity of criterion (iii) has also been proven by direct and large eddy simulations of channel flow of liquid metals [23]. A mixing length approach for the dissipation profile was used in that case to calculate the coefficient C_{T2} of the subgrid-scale heat flux model. Thus, these criteria increase the chance for the method of direct numerical simulation to be capable of predictions for any type of laminar and turbulent flow.

ACKNOWLEDGMENTS

The author wishes to thank Dr. U. Schumann, Professor F. H. Busse, and Professor J. W. Deardorff for stimulating comments. Mrs. Oberacker prepared the illustrations and Mrs. Stephany typed the manuscript.

REFERENCES

1. F. H. BUSSE, *in* "Hydrodynamic Instabilities and the Transition to Turbulence" (H. L. Swinney and J. P. Gollub, Eds.), p. 97, Springer Pub., New York, 1981.
2. F. B. LIPPS, *J. Fluid Mech.* **75** (1976), 113.
3. G. GRÖTZBACH, *J. Fluid Mech.* **119** (1982), 27
4. G. GRÖTZBACH, *Nucl. Eng. Design* **54** (1979), 49.
5. M. D. LOVE, *J. Inst. Nucl. Eng.* **20** (1979), 35.
6. U. SCHUMANN, G. GRÖTZBACH, AND L. KLEISER, *in* "Prediction Methods for Turbulent Flows" (W. Kollmann, Ed.), p. 123, Hemisphere Publ. Corp., Washington, 1980.
7. U. SCHUMANN, *J. Comput. Phys.* **18** (1975), 376.
8. M. ANTONOPOULOS-DOMIS, *J. Fluid Mech.* **104** (1981), 55.
9. B. J. DALY, *J. Fluid Mech.* **64** (1974), 129.
10. F. H. BUSSE, *Rep. Prog. Phys.* **41** (1978), 1929.
11. G. GRÖTZBACH, report KfK 2981 B, Kernforschungszentrum Karlsruhe, 1980.
12. G. E. WILLIS, J. W. DEARDROFF, AND R. C. J. SOMERVILLE, *J. Fluid Mech.* **54** (1972), 351.
13. R. M. CLEVER AND F. H. BUSSE, *Z. Ang. Math. Phys.* **29** (1978), 711.
14. J. W. DEARDORFF AND G. E. WILLIS, *J. Fluid Mech.* **28** (1967), 675.
15. F. H. BUSSE AND J. A. WHITEHEAD, *J. Fluid Mech.* **66** (1974), 67.
16. J. O. HINZE, "Turbulence," 2nd ed., Mc Graw–Hill, New York, 1975.
17. R. KRISHNAMURTI, *J. Fluid Mech.* **42** (1970), 309.
18. D. E. FITZJARRALD, *J. Fluid Mech.* **73** (1976), 693.
20. D. R. CHAPMAN, *AAIAA-J.* **17** (1979), 1293.
21. G. GRÖTZBACH, Thesis, University Karlsruhe, report KfK 2426, Kernforschungszentrum Karlsruhe, 1977. English translation in DOE-tr-61.
22. D. K. LILLY, *in* "Proc. IBM Scientific Comp. Symp. on Environmental Sciences," p. 195 IBM Form No. 320–1951, 1967.
23. G. GRÖTZBACH, *Int. J. Heat Mass Trans.* **24** (1981), 475.
24. G. GRÖTZBACH, *in* "Numerical Methods in Laminar and Turbulent Flow" (C. Taylor and B. A. Schreffler, Eds.), p. 593, Pineridge Press Ltd, Swansea, 1981.
25. J. P. GOLLUB AND S. V. BENSON, *J. Fluid Mech.* **100** (1980), 449.
26. R. KRISHNAMURTI, *J. Fluid Mech.* **60** (1973), 285.
27. D. C. THRELFALL, *J. Fluid Mech.* **67** (1975), 17.
28. I. CATTON, *in* "Proc. Sixth Int. Heat Transfer Conf.," p. 13, Toronto, 1978.
29. K. G. T. HOLLANDS, G. D. RAITHBY, AND L. KONICEK, *Int. J. Heat Mass Trans.* **18** (1975), 879.